Lawrence Berkeley National Laboratory
LBL Publications

Title

Design of Electrostatic Aberration Correctors for Scanning Transmission Electron Microscopy

Permalink

https://escholarship.org/uc/item/6f47r11v

Journal

Microscopy and Microanalysis, 29(6)

ISSN

Authors

Ribet, Stephanie M

Zeltmann, Steven E

Bustillo, Karen C

et al.

Publication Date

2023-12-21

DOI

Copyright Information

Peer reviewed

Design of Electrostatic Aberration Correctors for Scanning Transmission Electron Microscopy

Stephanie M Ribet, Steven E Zeltmann, Karen C Bustillo, Rohan Dhall, Peter Denes, Andrew M Minor, Roberto dos Reis, Vinayak P Dravid, Colin Ophus

DECTRIS

ARINA with NOVENA

Fast 4D STEM

DECTRIS NOVENA and CoM analysis of a magnetic sample.

Sample courtesy: Dr. Christian Liebscher, Max-Planck-Institut für Eisenforschung GmbH.
Experiment courtesy: Dr. Mingjian Wu and Dr. Philipp Pelz, Friedrich-Alexander-Universität, Erlangen-Nürnberg.

Design of Electrostatic Aberration Correctors for Scanning Transmission Electron Microscopy

Stephanie M. Ribet[1,2,3],*, Steven E. Zeltmann[4,5], Karen C. Bustillo[3], Rohan Dhall[3], Peter Denes[6], Andrew M. Minor[3,5], Roberto dos Reis[1,2,7], Vinayak P. Dravid[1,2,7], and Colin Ophus[3],*

[1]Department of Materials Science and Engineering, Northwestern University, Evanston, IL 60208, USA
[2]International Institute of Nanotechnology, Northwestern University, Evanston, IL 60208, USA
[3]National Center for Electron Microscopy, Molecular Foundry, Lawrence Berkeley National Laboratory, Berkeley, CA 94720, USA
[4]Platform for the Accelerated Realization, Analysis, and Discovery of Interface Materials (PARADIM), Cornell University, Ithaca, NY 14853, USA
[5]Department of Materials Science and Engineering, University of California, Berkeley, Berkeley, CA 94720, USA
[6]Molecular Foundry, Lawrence Berkeley National Laboratory, Berkeley, CA 94720, USA
[7]The NUANCE Center, Northwestern University, Evanston, IL 60208, USA
*Corresponding authors: Stephanie M. Ribet, E-mail: sribet@lbl.gov; Colin Ophus, E-mail: cophus@gmail.com

Abstract

In a scanning transmission electron microscope (STEM), producing a high-resolution image generally requires an electron beam focused to the smallest point possible. However, the magnetic lenses used to focus the beam are unavoidably imperfect, introducing aberrations that limit resolution. Modern STEMs overcome this by using hardware aberration correctors comprised of many multipole elements, but these devices are complex, expensive, and can be difficult to tune. We demonstrate a design for an electrostatic phase plate that can act as an aberration corrector. The corrector is comprised of annular segments, each of which is an independent two-terminal device that can apply a constant or ramped phase shift to a portion of the electron beam. We show the improvement in image resolution using an electrostatic corrector. Engineering criteria impose that much of the beam within the probe-forming aperture be blocked by support bars, leading to large probe tails for the corrected probe that sample the specimen beyond the central lobe. We also show how this device can be used to create other STEM beam profiles such as vortex beams and probes with a high degree of phase diversity, which improve information transfer in ptychographic reconstructions.

Key words: 4D-STEM, aberration correction, phase plate, scanning transmission electron microscopy, simulation

Introduction

Across biological and physical sciences, understanding material systems often requires precise characterization down to the nano or atomic scales. Scanning transmission electron microscopy (STEM) is a key tool to fulfill such requirements, as it has a small probe size that can be used for directly imaging structures and mapping of chemical and physical properties. In STEM, resolution is typically limited by spherical aberrations of the probe-forming lenses. These aberrations are unavoidable and intrinsic to the microscope design—Scherzer's theorem states that a static, rotationally symmetric magnetic field will always produce spherical aberrations greater than zero. However, Scherzer also pointed out that the resolution can be improved, despite these parasitic aberrations, by balancing defocus and spherical aberrations (Scherzer, 1936).

The importance of improving resolution in STEM by limiting aberrations has inspired a series of computational and physical advances that led to the design of multipole aberration correctors (Smith, 2008; Rose, 2009; Urban et al., 2022). Nowadays, these correctors have become more widespread, and researchers are routinely able to reach atomic resolution (Batson et al., 2002; Dahmen et al., 2009; Urban et al., 2022). Nonetheless, these devices can be expensive and complicated to operate, and there have been efforts to find alternative means

for aberration correction. Linck et al. (2017) incorporated a diffraction grating into the probe forming aperture of STEM such that the spherical aberrations were canceled in the first-order diffracted beam. Similarly, Roitman et al. (2021) used the thickness-dependent phase shift of silicon nitride thin-films to sculpt a phase plate that acts as an aberration corrector. These simpler devices helped to overcome some of the limitations of conventional aberration correctors, but deploying physical phase plates can be challenging in practice (Malac et al., 2021).

Programmable electrostatic phase plates, as demonstrated in an electron microscope by Verbeeck et al. (2018), are an exciting platform for direct control over the electron beam profile. The phase plate has multiple smaller apertures with individual voltage control, so each section has a different phase that can independently impart a shift on the electron beam before interaction with the sample. This concept allows for remarkable spatial control over the probe and can be tuned while inserted in the microscope. This approach to beam sculpting was proposed for aberration correction (Verbeeck et al., 2018) and further considered by Vega Ibáñez et al. (2023). These studies showed that a two terminal device is better than a one terminal device for aberration correction because a linear phase ramp can more readily match the aberration function profile with fewer apertures. In a follow-up
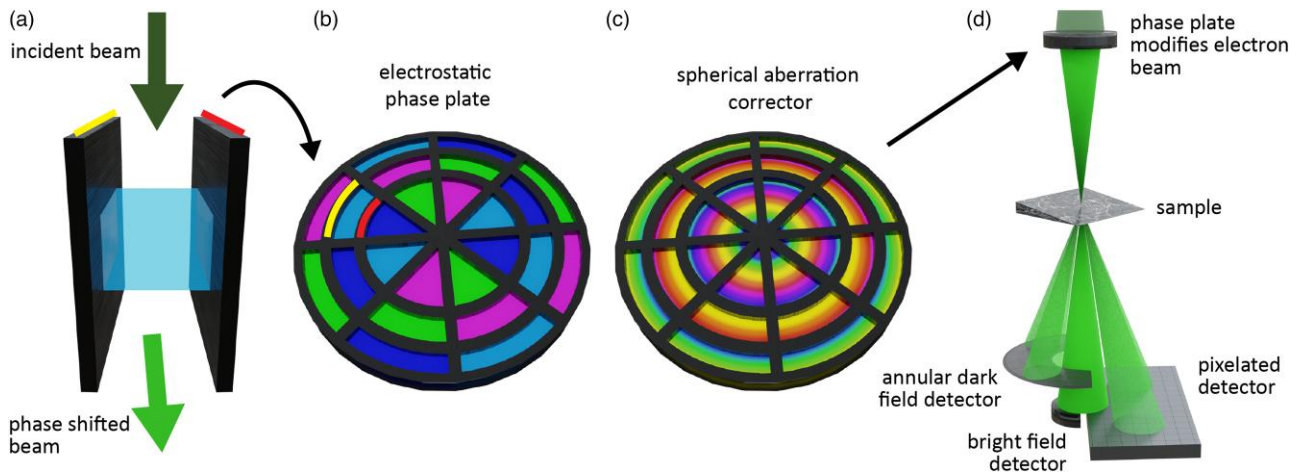
Fig. 1. (**a**) An electron beam is phase shifted when passed through an electrostatic potential. (**b**) A series of two-terminal devices can be arranged into a larger phase plate, where the potential in each aperture is tuned independently. Additional lines (red and yellow) in (**a**) and (**b**) denote terminals. (**c**) A potential difference between two terminals adds a linear phase ramp, which can be used to correct spherical aberrations. (**d**) The device is inserted in the probe forming aperture of the STEM to modify the electron beam before interaction with the sample and is compatible with imaging, diffraction, spectroscopy, and 4D-STEM experiments.

work, Vega Ibáñez et al. (2023) extended their design to include two terminals with independent voltages, in order to impart phase ramps to the electron beam, following earlier designs such as Boersch (1947), Matsumoto & Tonomura (1996), and Schultheiss et al. (2006).

In this work, we consider the implementation of a programmable phase plate (Fig. 1) and its impact on material characterization in light of realistic experimental constraints. We highlight the benefits of using such a device both for improving the STEM probe size and the limitations of this approach, mostly arising from the large probe tails due to architectural aperture supports. We illustrate how the programmable phase plate lends itself to the creation of other beam profiles. This device can be used to make a vortex beam or to impart phase diversity in the probe for better ptychographic reconstructions.

Theory

Here, we optimize the programmable phase plate specifically for correcting intrinsic spherical aberrations. Including only third-order spherical aberrations and defocus, the aberration function can be written as

$$\chi(q) = \frac{\pi}{2} C_3 \lambda^3 q^4 + \pi C_1 \lambda q^2, \tag{1}$$

where λ is the de-Broglie wavelength of the electron, C_3 is the third-order spherical aberration coefficient, and q is the spatial frequency. $C_1 = -\Delta f$, where Δf is the defocus. Examples of aberration functions for a microscope with and without defocus to balance the spherical aberrations are shown in Figure 2a. In STEM, the optimal conditions deviate slightly from the Scherzer conditions in TEM, as it is important to balance probe size with probe tails. Kirkland (1998) defines the best probe for STEM with the following equations:

$$C_1 = -0.87(C_3\lambda)^{1/2} \tag{2}$$

$$q_{\max} = 1.34(C_3\lambda^3)^{-1/4}. \tag{3}$$

In Figures 2a–2c, we are plotting simulations at 60 kV with a maximum scattering angle of 0.21 Å^{-1}. More details about

simulations throughout the study can be found in the Materials and Methods section. We use simulations to study the changes to the profile of the probe with aberrations, both with and without a corrector. These simulations do not include other complicating factors such as incoherence and higher-order aberrations in order to emphasize the impact of the phase plate. In reciprocal space, we can evaluate the efficacy of the transfer of information for various spatial frequencies by computing the contrast transfer function (CTF). The incoherent CTF is the Fourier transform of the normalized magnitude squared of the complex real space probe (Goodman, 2005). The CTF of an unaberrated lens has a value of 1 at zero spatial frequency and linearly decreased to zero at the spatial frequency corresponding to twice the semi-convergence angle of the probe (Fig. 2b). By balancing spherical aberrations with defocus, using the Scherzer condition in equation (2), the contrast transfer of information approaches the ideal profile. The maximum q or spatial frequency of information transfer corresponds to when the curve reaches CTF = 0, and the deviations from the ideal profile show a loss of efficiency.

There are also many heuristics for evaluating real space probe size that capture not only the radius of the central lobe but also the probe tails, which contribute parasitically to image contrast and resolution. Metrics that highlight information about the central lobe include the probe full width at half maximum and the radius containing 50% of current (Kirkland, 1998). Amplitude plates are known to create longer probe tails due to the constraint of missing spatial frequencies, so previous work describing bullseye-patterned apertures defined the STEM probe size as the radius containing 80% of the total probe intensity (Zeltmann et al., 2020). Finally, Schnitzer et al. (2020) used the Strehl ratio, the ratio of peak intensity between an aberrated and nonaberrated probe, to account for probe size. The real space probe profiles of the same probes are shown in Figure 2c. Again, we observe how balancing the spherical aberrations with defocus can improve the probe size.

Our design for a corrector is based on a two-terminal device that applies voltages on the order of $+/-10$V, which will be used to create a local electric field across an aperture, as shown in Figure 1a. A group of these apertures can be patterned into

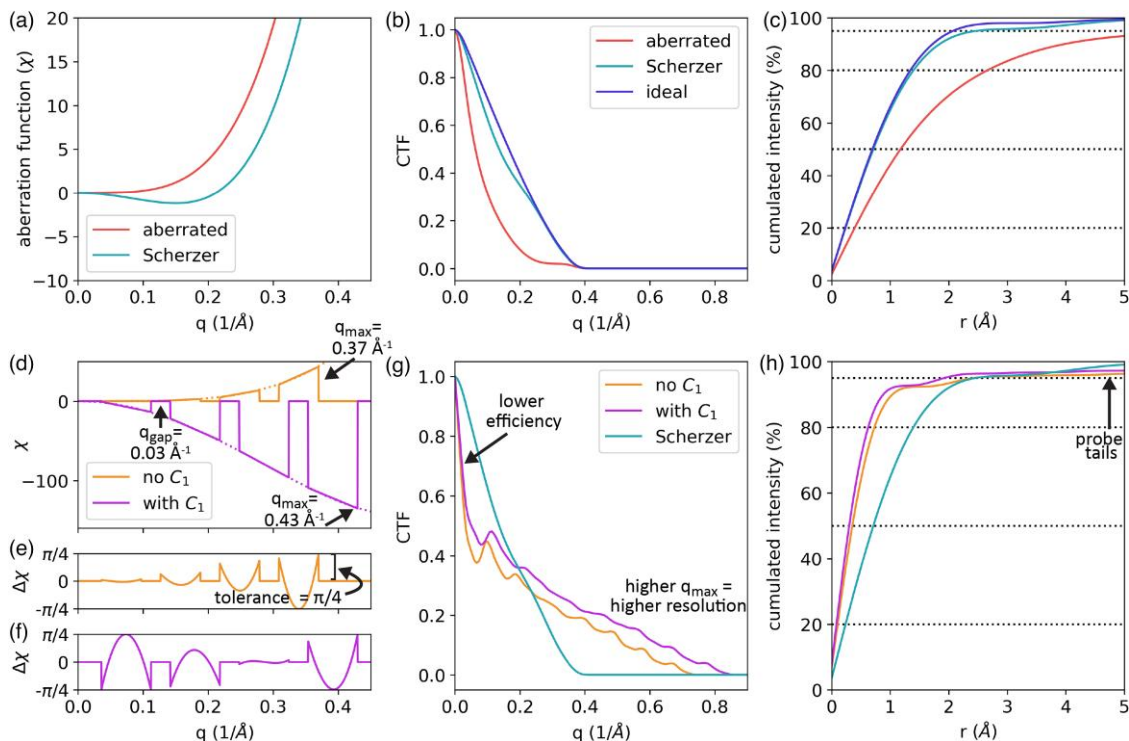**Fig. 2.** (**a**) Aberration functions for STEM probes at 60 kV which contain 1.3 mm C_3 spherical aberrations either with (Scherzer) and without defocus and (**b**) resulting CTFs and (**c**) cumulated probe intensity. C_1 can balance the C_3 aberrations to make a smaller probe. (**d**) Aberration functions and corrector profiles and residuals either (**e**) without and (**f**) with defocus. Adding C_1 helps extend the q_{max} of the device leading to a better (**g**) CTF and (**h**) probe profile.

an electrostatic phase plate (Fig. 1b). The size of the device is 100 s of μm with apertures on the order of 2–10 μm in the smallest dimension and is fabricated with standard silicon machining techniques. These apertures will have a linear phase profile, which can be used to approximate segments of the spherical aberration function to correct the probe (Fig. 1c). This phase plate will be inserted in the probe forming aperture of the microscope, in place of one of the C2 condenser apertures, to modify the electron beam before interaction with the sample as shown in Figure 1d.

In order to correct aberrations, our target corrector function should contain linearly ramping phase profiles that closely match the aberration function of the probe, with a negative sign to cancel these aberrations out. The phase error tolerance of the design determines how far out of phase electrons can be after they are corrected. Here, the tolerance is set as $\pi/4$ following conventional criteria (Kirkland, 1998; Weyland & Muller, 2020). Balancing spherical aberrations with defocus, we can minimize the curvature of the aberration function before applying the correction to improve the performance of the device. The aberration profile at higher spatial frequencies beyond the probe forming aperture will still depend most strongly on spherical aberration due to the q^4 relationship of this parameter (equation (1)). However, the defocus can help balance these aberrations at lower frequencies, similarly to how they are applied to reach Scherzer conditions. Starting with no defocus, we show the fit aberration function (Fig. 2d) and the residuals of a corrector (Fig. 2e). We plot the corresponding curves in Figures 2d and 2f for a corrector that includes defocus. Using a realistic crossbar width in the calculation, we can extend our maximum scattering angle from $q = 0.37\,\text{Å}^{-1}$ to $q = 0.43\,\text{Å}^{-1}$ by adding defocus. Note that both of these are larger maximum scattering angles than

could be achieved with the ideal Scherzer condition alone $(0.21\,\text{Å}^{-1})$.

Figure 2g shows the same Scherzer probe as in Figure 2b for reference. We can compare this profile to the corrected probes. At lower spatial frequencies, the corrected probes both are less efficient than the Scherzer probe. However, the corrected probes reach a higher maximum spatial frequency, which means that they will improve the resolution of the microscope. The programmable phase plate that includes defocus achieves higher resolution, due to the overall more linear aberration surface. Similarly, Figure 2h shows the improved real space profiles. Although the central lobe is much smaller, the corrected probes have larger tails, as evident in the radii containing more than 95% probe intensity.

The design of the aberration corrector plates resembles the device shown in Figure 3a. An ideal corrector would be free of cross bars and support rings, but such a design is not physically realizable. The fill factor is defined as:

$$\text{Fill factor} = \frac{\text{Unblocked area}}{\text{Blocked + unblocked area}}. \quad (4)$$

A smaller fill factor will mean more of the electron beam is blocked. The cross bars were chosen to have eightfold symmetry for more facile fabrication, but other support designs are possible. These parameters will ultimately depend on the physical size of the device and the resolution of the fabrication technique.

Figure 3a shows the overall schematic of our design. Red and yellow lines indicate (+) and (−) terminals, and the black support bars are insulating. Comparing Figures 3a and 3b highlights a key design choice in our programmable phase

plate. In Figure 3a, we block the center of the phase plate, which means that every aperture can have two terminals. By comparison, the design in Figure 3b has an open aperture in the center with a single electrode, as two electrodes in this circular aperture could not create a linearly ramping profile. The blocked center is the preferable choice, as it allows for more control over the electron beam profile. The color legend for this figure and the other probe plots throughout the article is shown in Figure 3c, and it shows that designs in both Figures 3a and 3b can largely remove aberrations in the probe. Figures 3d and 3e show the corresponding CTF and radial probe profiles for these two devices, illustrating the same degree of correction.

Next, we consider two approaches for determining the width of each aperture for the corrector: (1) evenly spaced apertures and (2) adaptively spaced apertures. Evenly spaced apertures were designed such that all the aperture widths are the same. The size of the device is increased until the corrected
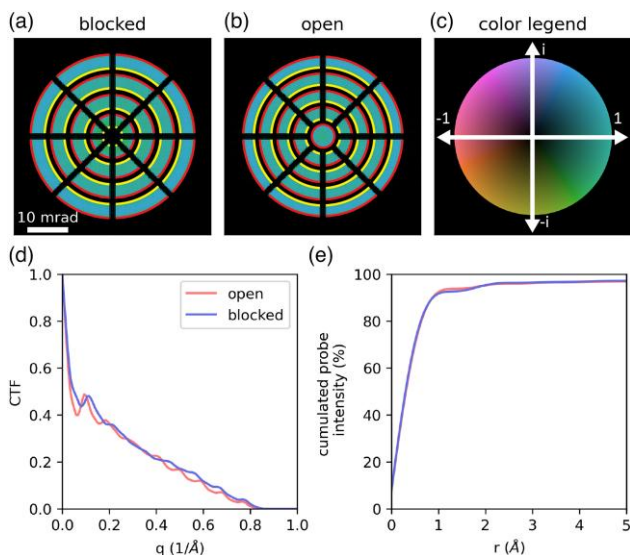
phase profile in any aperture reaches the tolerance of $\pi/4$. The aberration function and residuals for this method are plotted in Figures 4a and 4b, respectively. For adaptively spaced apertures, the width of each ring is determined independently, and its size is maximized such that the corrected phase profile in any aperture is within the tolerance of $\pi/4$ (Figs. 4a, 4c). Comparing the residuals in Figures 4b and 4c, we see why the adaptive corrector is the better choice. For the same number of rings, we achieve a higher maximum scattering angle.

Figure 4a highlights that the optimal defocus is not the same for these two designs, leading to different aberration function profiles. The challenge of finding the optimal defocus is difficult to solve analytically. This is especially true in the adaptive corrector cases, as the profile of maximum achievable scattering angle for various focus values oscillates. The optimal defocus for these devices was determined by starting at $C_1 = 0$ and progressively updating the defocus and calculating the maximum scattering angle. Once we reach a local maximum in scattering angle, we defined the best defocus and aperture size based on this maximum (Fig. 4d). Figure 4e shows the maximum achievable scattering angle for both approaches for different numbers of rings. With one ring, these two approaches yield the same degree of correction. However, for more rings, the adaptive corrector consistently performs better.

We next evaluate the parasitic contributions of probe tails for the two approaches. Figure 4f shows the radii containing 50% and 95% of the cumulated probe intensity. The 50% radius most closely corresponds to degree of correction or attainable resolution. As we add more rings to the corrector, we reach a higher scattering angle of corrected electrons, so the real space probe size improves. The adaptive corrector shows improved resolution over the evenly spaced corrector. The 95% intensity highlights another challenge with the evenly spaced corrector, namely broader probe tails. For a 4-ring device, we can plot these same metrics against fill factor using equation (4). As the fill factor gets lower the resolution stays nearly constant (50% intensity), while the probe tails, as represented by 95% intensity, increase. This illustrates a geometric consideration of the programmable phase plate, which is that as the support bars get larger, more spatial frequencies are missing, which creates larger probe tails.

To understand the limitations of the programmable corrector, we can also look at the profiles of the probes in real space. Figure 5 shows the profile of the probe along electron beam
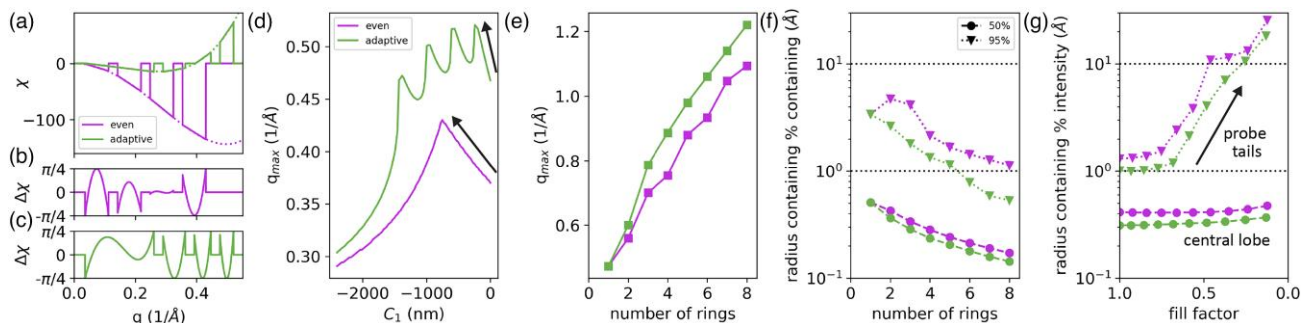

Fig. 3. Two possible designs for the aberration corrector are with a (**a**) blocked or (**b**) open center. The (**b**) open center design accommodates only a one terminal device in the central aperture limiting flexibility. (**c**) Argand plot showing legend for (**a**) and (**b**) and other probes in the article. The (**d**) CTF and (**e**) probe profiles for the two designs are similar. Simulations at 60 kV with 1.3 mm C_3.

Fig. 4. (**a**) Aberration function and corrector profile and residuals for (**b**) even and (**c**) adaptively spaced design. The adaptively spaced design leads to a higher q_{max}. (**d**) Both can be optimized by starting at 0 defocus and decreasing until the first maximum is reached. (**e**) As the number of rings is increased, so is the q_{max}. (**f**) As the number of rings is increased the radius containing 50% of the probe decreased due to the improve resolution for both the evenly and adaptively spaced correctors. The radius containing 95% of the probe is worse for the evenly spaced corrector. (**g**) Probe tails are more problematic as the fill factor is increased. Simulations at 60 kV with 1.3 mm C_3.
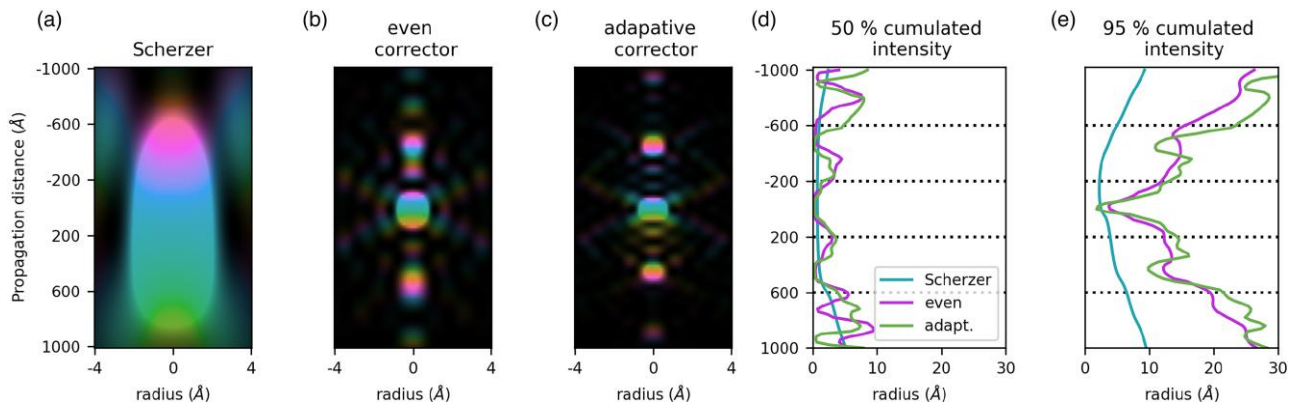
Fig. 5. Probe profiles of the (**a**) Scherzer condition and corrected probes with the (**b**) evenly spaced and (**c**) adaptively spaced phase plate. The color indicates phase using the legend in Figure 3c. Corrected probes have a smaller central lobe but modes above and below the plane of the sample. (**d**) 50% and (**e**) 95% probe profiles show long tails for the corrected probes. Simulations at 60 kV with 1.3 mm C_3.

propagation axis for (1) a Scherzer condition probe according to equation (2), (2) an evenly spaced corrected, and (3) adaptively spaced corrected probe in A–C, respectively. The 50% and 95% radial profiles of these probes are plotted in Figures 5d and 5e as well. While the corrected probes are much narrower, indicating a state of aberration correction, they have modes above and below the sample plane, which are similar to X-ray beam profiles in Fresnel zone plate experiments (Attwood, 2000). These extra modes would probe specimen information above and below the sample, which is an especially important consideration for thicker samples.

Figure 6 explores the performance of the device at various accelerating voltages at two values for spherical aberration: 1.3 mm, which is the range of spherical aberration coefficients for a high voltage S/TEM (Hong et al., 2021) and 5 mm, which is closer to the range for a low voltage scanning electron microscope (SEM) (Zach & Haider, 1995; Joy, 2008). The horizontal dashed lines represent the q_{max} achievable with balancing C_1 (equation (2)), while the solid profiles show the maximum achievable q_{max} for an adaptively spaced corrector of various number of rings. This figure underscores the choice of 60 kV as a goal for achieving atomic resolution. At 300 kV, the q_{max} is approaching 0.5 $Å^{-1}$, which would provide excellent atomic resolution imaging.

We also consider the possibility of using this type of corrector for an SEM. The results in Figure 6 suggest that although it may be possible to approach atomic resolution at 20 kV and 5 kV with a programmable phase plate, it would require many more apertures than at 60 kV, making the implementation of a programmable phase plate for aberration correction in an SEM challenging. Moreover, despite the spherical aberrations in an SEM being higher than in a STEM, the chromatic aberrations are more problematic. Thus there may be other challenges to achieving atomic resolution which this electrostatic phase plate corrector cannot address (Zach & Haider, 1995; Joy, 2008).

Materials and Methods

Unless otherwise noted, theory simulations are at 60 kV accelerating voltage with a C_3 of 1.3 mm. Low voltage S/TEM (60 kV) is intrinsically lower in resolution than higher voltage experiments, creating more incentive for aberration correction. This spherical aberration coefficient was chosen based on

realistic microscope parameters (Hong et al., 2021). When the phase plates are incorporated in simulated probes, no further modifications of the wavefunctions before the apertures are included, beyond the aberrations as indicated.

The graphene and silicon structures for these simulations were built from files available through the Materials Project (Jain et al., 2013). STEM simulations were performed using the *ab*TEM (Madsen & Susi, 2021) multislice code based on methods laid out by Kirkland (1998). Because two-dimensional materials need a high number of frozen phonon (FP) configurations to converge (DaCosta et al., 2021), twisted graphene bilayer simulations were run with 50 FPs, while tetracutinase and Si simulations were run with 12 FPs, and the standard deviation of the displacement was 0.1 Å. For the Moiré and Si simulations, the dark field detector was integrated from 80 to 135 mrad. Dark field (DF) and differential phase contrast (DPC) reconstructions were performed in *ab*TEM.

Simulations of tetracutinase (Parker et al., 2022) were performed in *ab*TEM. The probe was defocused to about 10 nm, and 4D datasets were simulated with a 1 nm step size to ensure sufficient probe overlap. Poisson noise was added to simulate a dose of 500e$^-$/Å^2. Ptychography refers to a family of phase retrieval techniques, where the phase of the sample and the probe are reconstructed from 4D-STEM datasets. Ptychographic reconstructions used the regularized ptychographic iterative engine algorithm as implemented in *ab*TEM (Maiden et al., 2017). 15 iterations were run with a step size of 0.1.

The Fourier ring correlation (FRC) is used to compute spatial frequencies transferred in image reconstructions (Van Heel & Schatz, 2005; Banterle et al., 2013).

$$FRC(r) = \frac{\sum_{r_i \in r} F_1(r) \cdot F_2(r)^*}{\sqrt{\sum_{r_i \in r} F_1^2(r) \cdot \sum_{r_i \in r} F_2^2(r)}}, \quad (5)$$

where F_1 and F_2 are the Fourier transforms of two real space reconstructions and * denotes the complex conjugate. Four reconstructions were calculated for each condition, and the FRCs were averaged to improve signal to noise. The half bit criteria define the signal to noise ratio at a given frequency, and the first intersection of the half bit curve (F(r)) with the FRC(r) with a negative slope of the difference curve defines
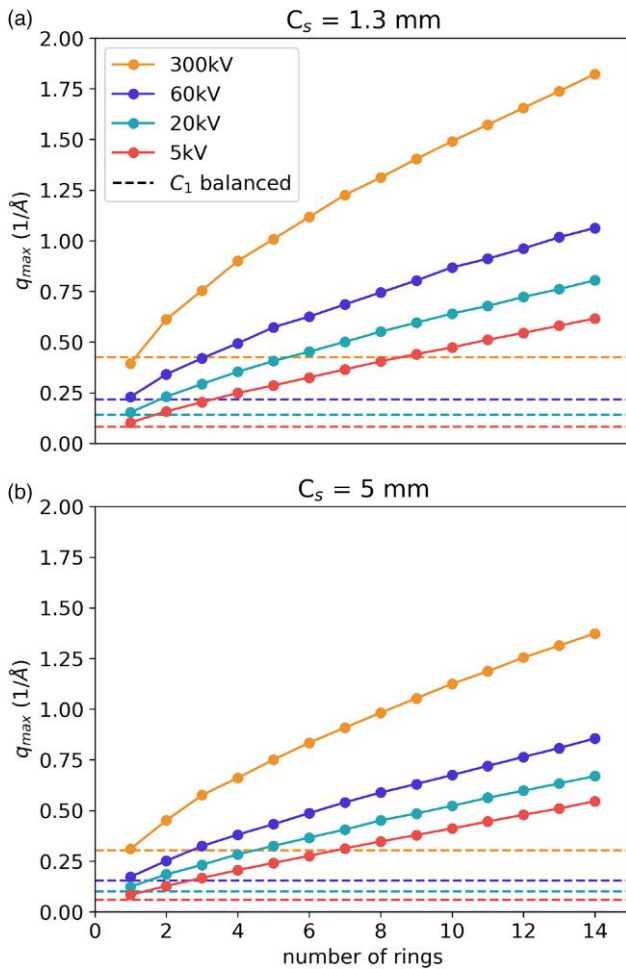
Fig. 6. Simulations of maximum scattering angle as a function of the number of rings for different voltages with (**a**) 1.3 mm C_3 and (**b**) 5 mm C_3 aberrated probes.

the resolution (Van Heel & Schatz, 2005; Banterle et al., 2013). The half-bit criteria are defined as

$$F(r) = \frac{2}{\sqrt{N(r)/2}}, \qquad (6)$$

where N(r) is the number of pixels in each ring.

Results

We use a Moiré graphene bilayer structure as a model system to test the performance of programmable phase plate as an aberration corrector. Figure 7a shows a dark field and differential phase contrast (DPC) image of the Moiré lattice under optimal conditions as described by equation (2). Because of the limited resolution of the probe in reciprocal space, it is not possible to resolve the fine features in the twisted graphene structure. However, Figures 7b and 7c shows simulations of the same structure with the evenly and adaptively spaced correctors. The adaptively spaced corrector performs slightly better than its evenly spaced counterpart, as it can reach higher maximum scattering angles ($q_{Scherzer} = 0.22$ Å^{-1}, $q_{even} = 0.51$ Å^{-1}, $q_{adaptive} = 0.63$ Å^{-1}).

We compare these results to an ideal probe with $q_{max} = 0.63$ Å^{-1} (Fig. 7d). Although the resolution is similar

to the images in Figures 7b and 7c, there is stronger contrast in the lattice. The CTFs in Figure 2 show reduced transfer of information with a phase plate corrector as compared to an ideal probe, especially at low spatial frequencies, so these images are in good agreement with the CTF calculations.

The limitations of the programmable phase plate approach to aberration correction are more clearly shown with a thicker sample. In Figure 8, we explore the impact of aberration correction on a 20 nm thick silicon sample oriented along the ⟨110⟩. Figure 8a shows the projected electron potential of the sample with the area of interest highlighted. We include a large vacuum region next to the sample, to emphasize the impact of the long probe tails. In Figure 8b, we show the image and line profile from a simulation with a perfect probe of scattering angle $q_{max} = 0.63$ Å^{-1}. We can clearly resolve the dumbbells and the intensity drops off within a few Ångströms of the edge of the sample.

We can compare these results to an image simulation with spherical aberrations and the corrector. We use a 5-ring programmable phase plate with the same q_{max} as Figure 8b. As shown previously, we would not be able to achieve atomic resolution for this aberrated probe without correction. With this corrector, we can successfully resolve the dumbbells in this sample. However, due to the long probe tails we see a strong background signal extending well into the vacuum. Even within 4 nm of the sample, the intensity has not dropped to zero, shown by the line profiles. Although the nominal central lobe size is sub-Ångström, the probe is sensitive to information nanometers away from the main area of illumination. Moreover, there is significantly reduced intensity at the atomic sites, similar to Figure 7. These probe tail features lower the contrast more in thicker samples due to beam broadening during beam-specimen interactions.

Here, we have described how the programmable phase plate can be used for spherical aberration correction. This hardware also allows for high flexibility in defining the electron beam wave function. For example, a Hilbert plate, where half of the beam is phase shifted by π can be used in TEM to improve contrast in studies of weak phase objects (Danev et al., 2002). Such a beam profile can be implemented with the programmable phase plate as shown in Figure 9a. There are many other types of phase plates that are more routinely used in TEM (Malac et al., 2021) but have been little explored in STEM. A programmable phase plate would allow for more testing of these usual beam profiles.

Vortex beams in S/TEM has been proposed for probing a number of material properties including chirality (Harvey et al., 2015; Juchtmans et al., 2015; Béché et al., 2017), symmetry (Juchtmans et al., 2016; Ribet et al., 2022), and magnetic structure (Verbeeck et al., 2010; Rusz & Bhowmick, 2013; Grillo et al., 2017). Figure 9 shows how these beams can be implemented in real and reciprocal space. The wave function of a vortex beam, $\Psi_v(q)$, is defined by:

$$\Psi_v(q) = \Psi(q)e^{im\phi} \qquad (7)$$

Here, $\Psi(q)$ is the wave function of an unmodified beam, m is the quantum number, and ϕ is the azimuthal coordinates with respect to the propagation direction of the electron beam. Energy-loss magnetic circular dichroism (EMCD) experiments, for example, probe magnetic order with a chiral vortex beam (Schattschneider et al., 2006; Verbeeck et al., 2010). In such an experiment, one needs to compare an
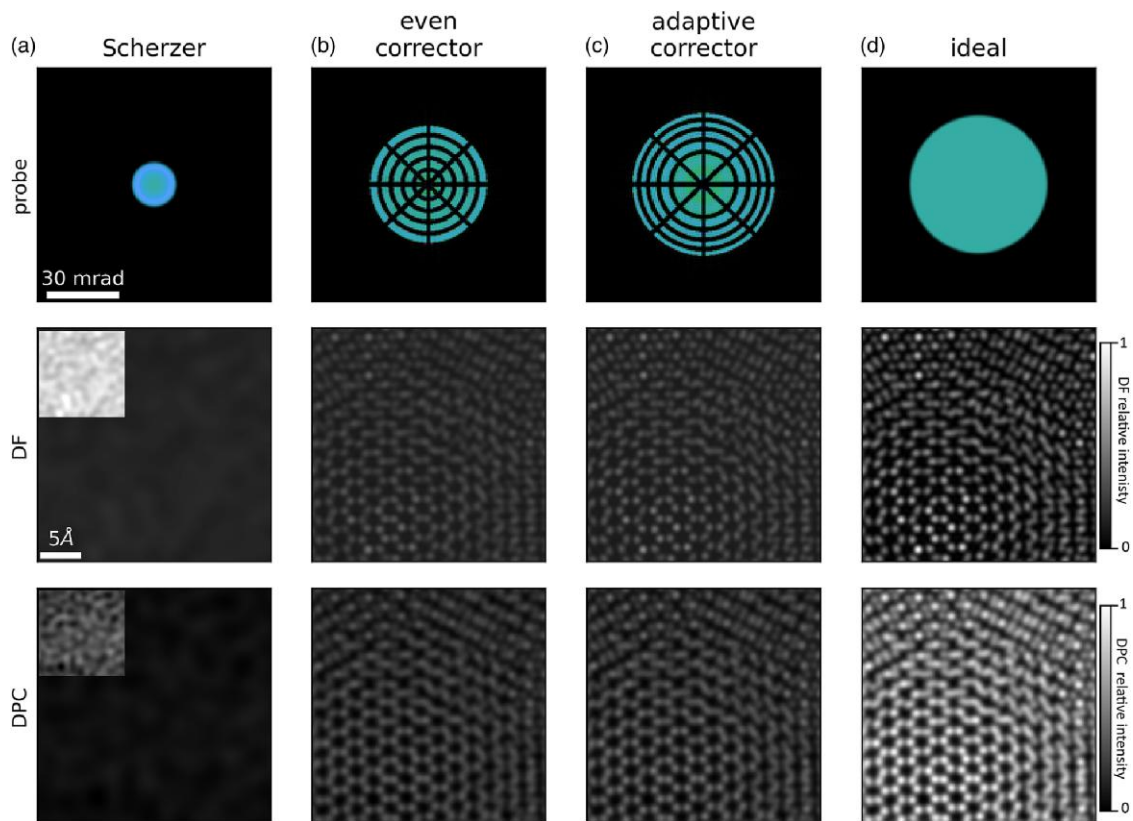
Fig. 7. (**a**) The Scherzer condition probe does not provide sufficient resolution for imaging of twisted bilayer graphene. Inset shows reconstructions with 5x smaller contrast range, highlighting that the Scherzer probe captures only noise. The (**b**) evenly spaced and (**c**) adaptively spaced corrected probes provide atomic resolution images. Compared to an (**d**) ideal probe the efficiency is reduced in the corrected images as shown by the lower contrast. Simulations at 60 kV with 1.3 mm C_3 with $q_{max} = 0.22$ Å^{-1}, $q_{max} = 0.51$ Å^{-1}, $q_{max} = 0.63$ Å^{-1} and $q_{max} = 0.63$ Å^{-1} in a–d, respectively.

electron energy loss experiment from the same area with a $m = +1$ and $m = -1$ beam, which can be challenging to implement experimentally. A programmable phase plate can be used to make a vortex beam, as shown in Figure 9b, and the tunable nature of this design lends itself to EMCD experiments.

Finally, our programmable phase plate could be used for adding phase diversity in a STEM probe for ptychographic reconstructions. Ptychography experiments are often performed in a defocused probe configuration, which adds phase in the incident beam (Rodenburg & Maiden, 2019). However, there have been a variety of studies that have suggested that adding additional phase diversity into the probe, including dynamic phase, can help with more efficient reconstructions, especially at low spatial frequencies (Candes et al., 2015; Yang et al., 2016; Pelz et al., 2017; Allars et al., 2021). A programmable phase plate would be well suited to add phase into the probe for ptychography experiments.

Using tetracutinase a model system, we explore this phase plate configuration, and in particular how adding phase diversity can be used to improve the information transfer for defocused probe ptychographic reconstructions. Similar to many biological structures, these megamolecules are weak phase objects and beam sensitive, making low dose ptychography a good approach to imaging these materials (Parker et al., 2022). Figure 10a shows the projected potential of this small four-lobed molecule. The reconstructions using an ideal probe with 2.5 mrad and 10 mrad convergence angles (Figs. 10b, 10c, respectively) show the impact of convergence angle on the reconstruction.

At a smaller convergence angle, the low spatial frequency information is captured, while the larger convergence angle results in an image that appears high-pass filtered. The FRC plots (Fig. 10e) show improved resolution for the larger convergence angle. These reconstructions are in agreement with the images and experimental results from the literature (Zhou et al., 2020).

Figure 10d shows the STEM phase plate that we use for this simulation. This design was chosen to incorporate phase diversity in the probe. The ptychographic reconstruction using this probe wave function is shown in Figure 10e. The image reflects a wider range of spatial frequencies—the low spatial frequency information is preserved while capturing the fine detail in the megamolecule's lobes. In addition, these reconstructions are more robust in the vacuum region to systematic errors. The FRC profile for this reconstruction shows the same resolution as compared to the conventional 10 mrad probe, but with improved transfer at lower spatial frequencies. Overall, these simulations suggest that incorporating phase diversity into an incident probe can improve ptychographic reconstructions.

Discussion

Lastly, we discuss experimental implementation of the phase plate and practical considerations of how it is different from a conventional aberration corrector. A multipole corrector is a much more complicated device that corrects higher-order aberrations in addition to the spherical aberrations which are
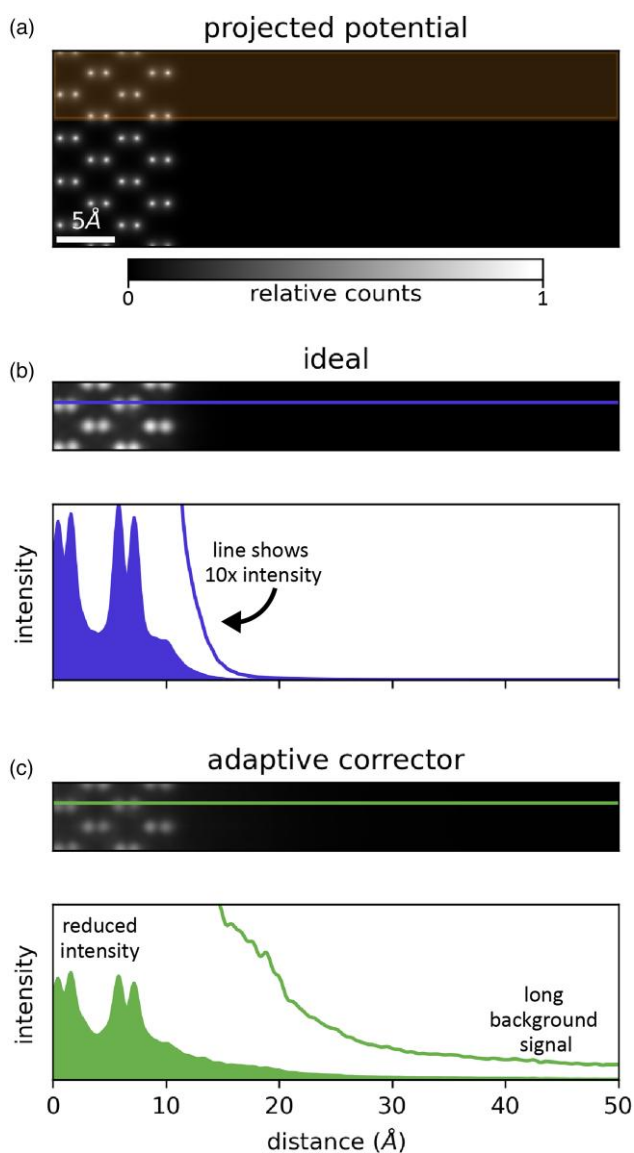
(a)

projected potential

5Å

0   relative counts   1

(b)

ideal

intensity

line shows
10x intensity

(c)

adaptive corrector

intensity

reduced
intensity

long
background
signal

0   10   20   30   40   50
distance (Å)

Fig. 8. (**a**) Projected potential of a 20 nm Si sample. Comparing the (**b**) perfect probe and (**c**) corrected probe, we observe that despite the benefits of the programmable phase plate for improving resolution, there is a cost of reduced intensity and strong background signal. Simulations at 60 kV with 1.3 mm C_3.

(a)   reciprocal space   real space

hilbert

10 mrad   5 Å

(b)

vortex, $m = 1$

(c)

vortex, $m = 2$

Fig. 9. A programmable phase plate allows for the implementation of more exotic beam profiles including (**a**) a probe with a Hilbert plate or a vortex beam with (**b**) $m = 1$ or (**c**) $m = 2$.

discussed here. Multipole elements introduce higher-order aberrations themselves, which need to be corrected (Kirkland, 1998; Müller et al., 2006).

In this work, we have only considered the correction of round aberrations, as C3 is typically the limiting aberration. Once C3 has been suitably compensated for, the next limiting aberrations are likely the first and second order nonround aberrations: A1, A2, and B2. As our design does not introduce any new multipole elements into the optics, it does not produce parasitic aberrations that require tuning. However, this device is less suited to compensate for nonround aberrations than a conventional corrector because, within each segment, we are able to produce a phase ramp only in the radial direction. Some tuning of nonround aberrations is likely possible by varying the mean potential within each segment along the azimuthal direction, but we expect to primari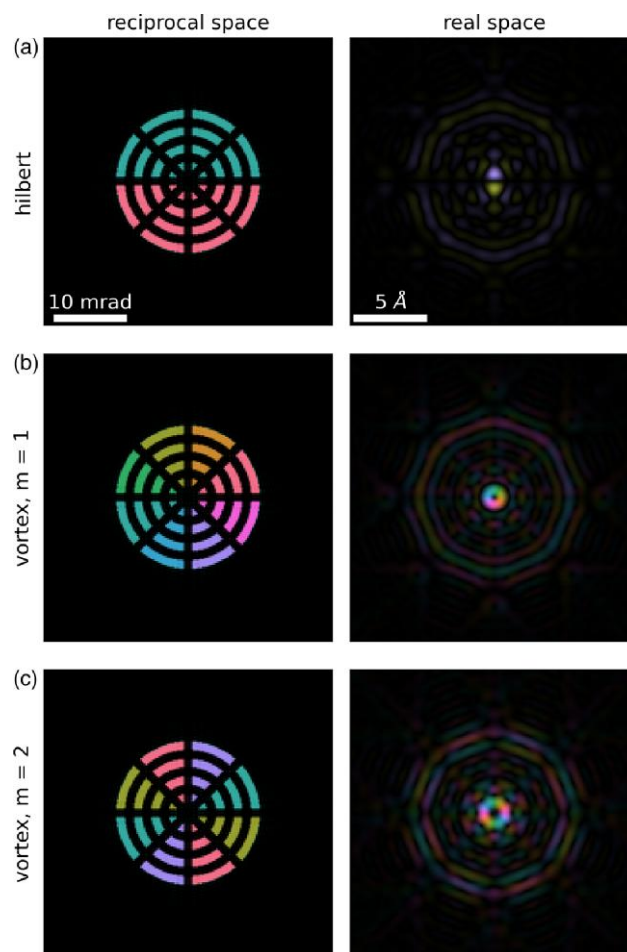ly rely on the stigmators and deflectors that are already available in a standard TEM column. Intrinsic fifth-order spherical aberrations could be corrected with a similar phase plate design.

We expect that the ideal wavefunction before the phase plate will have these nonround aberrations minimized. As our corrector sits in the condenser aperture of the microscope, it is possible to fully remove it from the beam path and perform standard Ronchigram tuning before inserting the phase plate. The simulations in this work provide the first guess at the correct excitation for each element as a function of the desired C3 correction. Nonetheless, we anticipate the need to incorporate software modules to adjust our apertures, as computational advances were pivotal in the implementation of multipole correctors (Rose, 2009). We plan to use an iterative approach where individual segments are varied one at a time, both to measure the response function and to minimize the probe size.

Our phase plate uses many orders of magnitude of power less than a conventional corrector, which suggests less concern about thermal drift and voltage stability. Multipole correctors are also far more nonlinear, since all the elements are in series with complicated couplings between stages that affect aberrations (Rose, 2009). In our design, elements are in parallel, so drift might be expected to compound differently.
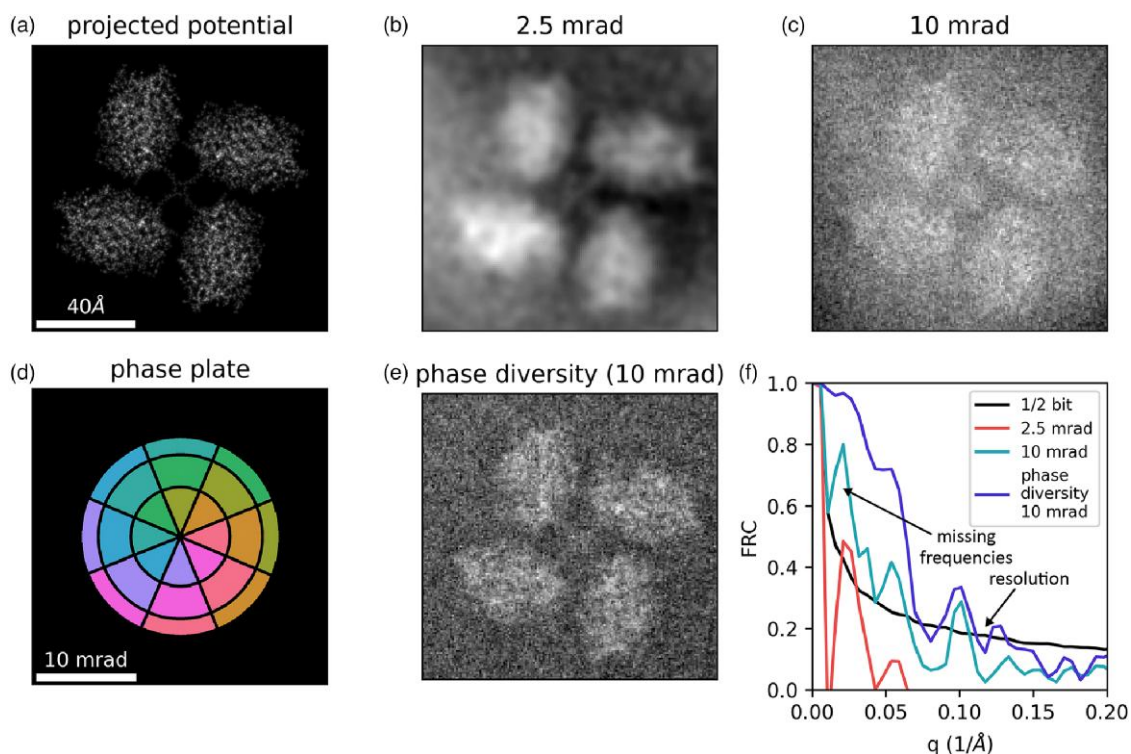
Fig. 10. (**a**) Projected potential of tetracutinase and defocused ptychography reconstructions with (**b**) 2.5 and (**c**) 10 mrad defocused probes. A (**d**) phase plate adds diversity to the (**e**) reconstructions, which capture a wider range of spatial frequencies. (**f**) FRC profiles evaluate transfer of information in these experiments.

Despite the benefits in terms of cost and simplicity in our design, one significant challenge is the long probe tails, which will ultimately limit the practical probe size. Beyond the applications of aberration correction, this design can also provide more flexibility in the phase profile of the beam by way of discontinuous segments that can be tuned independently. Vortex beams and other exotic probes allow for characterization of the structure and property of materials that would not be accessible in conventional experiments. Combining these two devices, a conventional multipole corrector could remove aberrations, and a programmable phase plate could sculpt the probe profile.

Conclusion

We have shown how to design a programmable phase plate for spherical aberration correction in light of realistic design criteria. We have illustrated how this device can be used to correct third-order spherical aberrations to produce atomic-resolution images. One of the key limitations of these devices is that the probe will have long tails that sample beyond the central lobe. A programmable phase plate can be used to create more complex probe profiles, such as a vortex beam. We have shown how these types of beam profiles can add phase diversity to improve transfer of information in ptychographic reconstructions.

Acknowledgments

Competing Interests

The authors declare that they have no competing interests.

References

Allars F, Lu P-H, Kruth M, Dunin-Borkowski RE, Rodenburg JM & Maiden AM (2021). Efficient large field of view electron phase imaging

using near-field electron ptychography with a diffuser. *Ultramicroscopy* **231**, 113257. https://doi.org/10.1016/j.ultramic.2021.113257

Attwood D (2000). *Soft X-rays and Extreme Ultraviolet Radiation: Principles and Applications*. Cambridge, United Kingdom: Cambridge University Press.

Banterle N, Bui KH, Lemke EA & Beck M (2013). Fourier ring correlation as a resolution criterion for super-resolution microscopy. *J Struct Biol* **183**(3), 363–367. https://doi.org/10.1016/j.jsb.2013.05.004

Batson PE, Dellby N & Krivanek OL (2002). Sub-ångstrom resolution using aberration corrected electron optics. *Nature* **418**(6898), 617–620. https://doi.org/10.1038/nature00972

Béché A, Juchtmans R & Verbeeck J (2017). Efficient creation of electron vortex beams for high resolution stem imaging. *Ultramicroscopy* **178**, 12–19. https://doi.org/10.1016/j.ultramic.2016.05.006

Boersch H (1947). Über die kontraste von atomen im elektronenmikroskop. *Zeitschrift Naturforschung A* **2**(11-12), 615–633. https://doi.org/10.1515/zna-1947-11-1204

Candes EJ, Li X & Soltanolkotabi M (2015). Phase retrieval from coded diffraction patterns. *Appl Comput Harmon Anal* **39**(2), 277–299. https://doi.org/10.1016/j.acha.2014.09.004

DaCosta LR, Brown HG, Pelz PM, Rakowski A, Barber N, O'Donovan P, McBean P, Jones L, Ciston J, Scott M & Ophus C (2021). Prismatic 2.0–simulation software for scanning and high resolution transmission electron microscopy (STEM and HRTEM). *Micron* **151**, 103141. https://doi.org/10.1016/j.micron.2021.103141

Dahmen U, Erni R, Radmilovic V, Ksielowski C, Rossell M-D & Denes P (2009). Background, status and future of the transmission electron aberration-corrected microscope project. *Philos Trans R Soc A: Math Phys Eng Sci* **367**(1903), 3795–3808. https://doi.org/10.1098/rsta.2009.0094

Danev R, Okawara H, Usuda N, Kametani K & Nagayama K (2002). A novel phase-contrast transmission electron microscopy producing high-contrast topographic images of weak objects. *J Biol Phys* **28**(4), 627–635. https://doi.org/10.1023/A:1021234621466

Goodman JW (2005). *Introduction to Fourier Optics*. Englewood, CO, United States: Roberts and Company Publishers.

Grillo V, Harvey TR, Venturi F, Pierce JS, Balboni R, Bouchard F, Carlo Gazzadi G, Frabboni S, Tavabi AH, Li Z-A, Dunin-Borkowski RE, Boyd RW, McMorran BJ & Karimi E (2017). Observation of nanoscale magnetic fields using twisted electron beams. *Nat Commun* **8**(1), 1–6. https://doi.org/10.1038/s41467-016-0009-6

Harvey TR, Pierce JS, Chess JJ & McMorran BJ (2015). Demonstration of electron helical dichroism as a local probe of chirality. arXiv preprint arXiv:1507.01810. https://doi.org/10.48550/arXiv.1507.01810

Hong X, Zeltmann SE, Savitzky BH, DaCosta LR, Müller A, Minor AM, Bustillo KC & Ophus C (2021). Multibeam electron diffraction. *Microsc Microanal* **27**(1), 129–139. https://doi.org/10.1017/S1431927620024770

Jain A, Ong SP, Hautier G, Chen W, Richards WD, Dacek S, Cholia S, Gunter D, Skinner D, Ceder G & Persson KA (2013). The materials project: A materials genome approach to accelerating materials innovation. *APL Mater* **1**(1), 011002. https://doi.org/10.1063/1.4812323

Joy DC (2008). The aberration-corrected SEM. In *Biological Low-Voltage Scanning Electron Microscopy*, pp. 107–127. New York, NY, United States: Springer.

Juchtmans R, Béché A, Abakumov A, Batuk M & Verbeeck J (2015). Using electron vortex beams to determine chirality of crystals in transmission electron microscopy. *Phys Rev B* **91**(9), 094112. https://doi.org/10.1103/PhysRevB.91.094112

Juchtmans R, Guzzinati G & Verbeeck J (2016). Extension of Friedel's law to vortex-beam diffraction. *Phys Rev A* **94**(3), 033858. https://doi.org/10.1103/PhysRevA.94.033858

Kirkland EJ (1998). *Advanced Computing in Electron Microscopy*. vol. **12**. Cham, Switzerland: Springer.

Linck M, Ercius PA, Pierce JS & McMorran BJ (2017). Aberration corrected stem by means of diffraction gratings. *Ultramicroscopy* **182**, 36–43. https://doi.org/10.1016/j.ultramic.2017.06.008

Madsen J & Susi T (2021). The abTEM code: Transmission electron microscopy from first principles. *Open Res Europe* **1**(24), 24. https://doi.org/10.12688/openreseurope

Maiden A, Johnson D & Li P (2017). Further improvements to the ptychographical iterative engine. *Optica* **4**(7), 736–745. https://doi.org/10.1364/OPTICA.4.000736

Malac M, Hettler S, Hayashida M, Kano E, Egerton RF & Beleggia M (2021). Phase plates in the transmission electron microscope: Operating principles and applications. *Microscopy* **70**(1), 75–115. https://doi.org/10.1093/jmicro/dfaa070

Matsumoto T & Tonomura A (1996). The phase constancy of electron waves traveling through Boersch's electrostatic phase plate. *Ultramicroscopy* **63**(1), 5–10. https://doi.org/10.1016/0304-3991(96)00033-2

Müller H, Uhlemann S, Hartel P & Haider M (2006). Advancing the hexapole Cs-corrector for the scanning transmission electron microscope. *Microsc Microanal* **12**(6), 442–455. https://doi.org/10.1017/S1431927606060600

Parker KA, Ribet S, Kimmel BR, Dos Reis R, Mrksich M & Dravid VP (2022). Scanning transmission electron microscopy in a scanning electron microscope for the high-throughput imaging of biological assemblies. *Biomacromolecules* **23**(8), 3235–3242. https://doi.org/10.1021/acs.biomac.2c00323

Pelz PM, Qiu WX, Bücker R, Kassier G & Miller R (2017). Low-dose cryo electron ptychography via non-convex Bayesian optimization. *Sci Rep* **7**(1), 1–13. https://doi.org/10.1038/s41598-017-07488-y

Ribet SM, Ophus C, dos Reis R & Dravid VP (2022). Dose-efficient defect contrast with 4D-STEM. *Microsc Microanal* **28**(S1), 346–348. https://doi.org/10.1017/S1431927622002148

Rodenburg J & Maiden A (2019). Ptychography. In *Springer Handbook of Microscopy*, pp. 819–904. Cham, Switzerland: Springer.

Roitman D, Shiloh R, Lu P-H, Dunin-Borkowski RE & Arie A (2021). Shaping of electron beams using sculpted thin films. *ACS Photonics* **8**(12), 3394–3405. https://doi.org/10.1021/acsphotonics.1c00951

Rose H (2009). History of direct aberration correction. In *Advances in Imaging and Electron Physics: Aberration-corrected Electron Microscopy*, pp. 1. Amsterdam, The Netherlands: Academic Press.

Rusz J & Bhowmick S (2013). Boundaries for efficient use of electron vortex beams to measure magnetic properties. *Phys Rev Lett* **111**(10), 105504. https://doi.org/10.1103/PhysRevLett.111.105504

Schattschneider P, Rubino S, Hébert C, Rusz J, Kuneš J, Novák P, Carlino E, Fabrizioli M, Panaccione G & Rossi G (2006). Detection of magnetic circular dichroism using a transmission electron microscope. *Nature* **441**(7092), 486–488. https://doi.org/10.1038/nature04778

Scherzer O (1936). Über einige fehler von elektronenlinsen. *Zeitschrift Physik* **101**(9-10), 593–603. https://doi.org/10.1007/BF01349606

Schnitzer N, Sung SH & Hovden R (2020). Optimal STEM convergence angle selection using a convolutional neural network and the Strehl ratio. *Microsc Microanal* **26**(5), 921–928. https://doi.org/10.1017/S1431927620001841

Schultheiss K, Pérez-Willard F, Barton B, Gerthsen D & Schröder R (2006). Fabrication of a Boersch phase plate for phase contrast imaging in a transmission electron microscope. *Rev Sci Instrum* **77**(3), 033701. https://doi.org/10.1063/1.2179411

Smith DJ (2008). Development of aberration-corrected electron microscopy. *Microsc Microanal* **14**(1), 2–15. https://doi.org/10.1017/S1431927608080124

Urban KW, Barthel J, Houben L, Jia C-L, Jin L, Lentzen M, Mi S-B, Thust A & Tillmann K (2022). Progress in atomic-resolution aberration corrected conventional transmission electron microscopy (CTEM). *Prog Mater Sci* **133**, 101037. https://doi.org/10.1016/j.pmatsci.2022.101037

Van Heel M & Schatz M (2005). Fourier shell correlation threshold criteria. *J Struct Biol* **151**(3), 250–262. https://doi.org/10.1016/j.jsb.2005.05.009

Vega Ibáñez F, Béché A & Verbeeck J (2023). Can a programmable phase plate serve as an aberration corrector in the transmission

electron microscope (TEM)? *Microsc Microanal* **29**(1), 341–351. https://doi.org/10.1017/S1431927622012260

Verbeeck J, Béché A, Müller-Caspary K, Guzzinati G, Luong MA & Den Hertog M (2018). Demonstration of a 2×2 programmable phase plate for electrons. *Ultramicroscopy* **190**, 58–65. https://doi.org/10.1016/j.ultramic.2018.03.017

Verbeeck J, Tian H & Schattschneider P (2010). Production and application of electron vortex beams. *Nature* **467**(7313), 301–304. https://doi.org/10.1038/nature09366

Weyland M & Muller DA (2020). Tuning the convergence angle for optimum stem performance. arXiv preprint arXiv:2008.12870. https://doi.org/10.48550/arXiv.2008.12870

Yang H, Ercius P, Nellist PD & Ophus C (2016). Enhanced phase contrast transfer using ptychography combined with a pre-specimen phase plate in a scanning transmission electron microscope. *Ultramicroscopy* **171**, 117–125. https://doi.org/10.1016/j.ultramic.2016.09.002

Zach J & Haider M (1995). Aberration correction in a low voltage SEM by a multipole corrector. *Nucl Instrum Methods Phys Res Sect A: Accel Spectrom Detect Assoc Equip* **363**(1-2), 316–325. https://doi.org/10.1016/0168-9002(95)00056-9

Zeltmann SE, Müller A, Bustillo KC, Savitzky B, Hughes L, Minor AM & Ophus C (2020). Patterned probes for high precision 4D-STEM bragg measurements. *Ultramicroscopy* **209**, 112890. https://doi.org/10.1016/j.ultramic.2019.112890

Zhou L, Song J, Kim JS, Pei X, Huang C, Boyce M, Mendonça L, Clare D, Siebert A, Allen CS, Liberti E, Stuart D, Pan X, Nellist PD, Zhang P, Kirkland AI & Wang P (2020). Low-dose phase retrieval of biological specimens using cryo-electron ptychography. *Nat Commun* **11**(1), 2773. https://doi.org/10.1038/s41467-020-16391-6